Nuclear Science and Engineering

ISSN: (Print) (Online) Journal homepage: https://www.tandfonline.com/loi/unse20

Computational Fluid Dynamics Analysis of an Open-Pool Nuclear Research Reactor Core for Fluid Flow Optimization Using a Channel Box

N. L. Scuro, G. Angelo, E. Angelo, M. H. A. Piro, P. E. Umbehaun, W. M. Torres & D. A. Andrade

To cite this article: N. L. Scuro, G. Angelo, E. Angelo, M. H. A. Piro, P. E. Umbehaun, W. M. Torres & D. A. Andrade (2023) Computational Fluid Dynamics Analysis of an Open-Pool Nuclear Research Reactor Core for Fluid Flow Optimization Using a Channel Box, Nuclear Science and Engineering, 197:6, 1100-1116, DOI: 10.1080/00295639.2022.2142437

To link to this article: https://doi.org/10.1080/00295639.2022.2142437

Published online: 15 Dec 2022.

NUCLEAR SCIENCE AND ENGINEERING · VOLUME 197 · 1100–1116 · JUNE 2023

DOI: https://doi.org/10.1080/00295639.2022.2142437

Computational Fluid Dynamics Analysis of an Open-Pool Nuclear Research Reactor Core for Fluid Flow Optimization Using a Channel Box

N. L. Scuro,[a,b]* G. Angelo,[c] E. Angelo,[c] M. H. A. Piro,[b] P. E. Umbehaun,[a] W. M. Torres,[a] and D. A. Andrade[a]

[a]*Nuclear and Energy Research Institute, Nuclear Engineering Center, São Paulo, Brazil*
[b]*Ontario Tech University, Department of Energy and Nuclear Engineering, Oshawa, Ontario, Canada*
[c]*Mackenzie Presbyterian University, School of Engineering, São Paulo, Brazil*

Received May 10, 2022
Accepted for Publication October 26, 2022

Abstract — *A channel box installation in the IEA-R1 research reactor core was numerically investigated to increase fluid flow in fuel assemblies (FAs) and side water channels (SWCs) between FAs by minimizing bypasses in specific regions of the reactor core, which is expected to reduce temperatures and oxidation effects in lateral fuel plates (LFPs). To achieve this objective, an isothermal three-dimensional computational fluid dynamics model was created using Ansys CFX to analyze fluid flow distribution in the Brazilian IEA-R1 research reactor core. All regions of the core and realistic boundary conditions were considered, and a detailed mesh convergence study is presented. Results comparing both scenarios are presented in the percentage of use of the primary circuit pump. It is indicated that 21.4% of fluid bypass to unnecessary regions can be avoided with the channel box installation, which leads to the total mass flow from the primary circuit for all FAs increasing from 68.9% (without a channel box) to 77.6% (with a channel box). For the SWCs, responsible for cooling LFPs, an increment from 9.7% to 22.4%, avoiding all nondesired cross three-dimensional effects, was observed, resulting in a more homogeneous fluid flow and vertical velocities. It was concluded that the installation of a channel box numerically indicates an expressive mass flow increase and homogeneous fluid flow distribution for flow dynamics in relevant regions. This gives greater confidence to believe that lower temperatures, and consequently oxidation effects in LFPs, can be expected with a channel box installation.*

Keywords — *Research reactor core, flow distribution optimization, computational fluid dynamics, channel box.*

Note — *Some figures may be in color only in the electronic version.*

I. INTRODUCTION

There are 45 pool-type research reactors in full operation,[1] and they are normally cooled with demineralized light water and can be designed with either positive pressure within the elements (upstream coolant flow) or relative negative pressure (downstream coolant flow). For reactors with downstream flow, some specific scenarios may take place. Flow reversal from downward to upward flow occurs after reactor shutdown or in the event of a loss-of-coolant accident[2] due to the transition from forced convection to natural convection.[3] During this process, depending on the intensity of the decay,[4] the fuel assembly (FA) may exhibit temperature peaks higher than steady-state temperature,[5] which may result in the onset of a two-phase flow behavior for a short period of time.[6]

A second issue may be related to the geometry and design of the reactor core. As an example, the IEA-R1 Brazilian research reactor core, located at Instituto de

*E-mail: nikolas.scuro@gmail.com

Pesquisas Energéticas e Nucleares (IPEN) in São Paulo, Brazil, is illustrated in Fig. 1. The core is composed of 20 standard fuel assemblies (SFAs), highlighted in red, four control fuel assemblies (CFAs), and other components such as reflectors and irradiation elements, shown in a simplified way. All core elements are open-to-pool and with no structure guiding fluid flow from upstream to downstream in side water channels (SWCs), which is the space between lateral fuel plates (LFPs) between all FAs present in the core. In addition, there are other regions where flow bypass may take place, which can reduce flow from entering FAs, contributing to an increase in temperature and possibly oxidation effects.

The present study is part of an extensive investigation of the fluid dynamics of the IEA-R1's research reactor core. Previously, the flow dynamics inside SFAs gave enough details about flow distribution between fuel plates.[7] The present study is a second investigation step, which focuses on analyzing the influence of bypasses and flow distribution among all FAs in the core. This investigation started after 1993 when several modifications were made to the original 1957 IEA-R1 core design. Among them, the original pump was substituted with a 13.3% more powerful primary circuit pump (681 to 772 m^3/h), the total number of FAs was reduced from 30 to 24, and thermal power was increased from 2 to 5 MW, resulting in a higher power density[8] and neutron flux to address local Brazilian demand for radioisotope production and academic research.

Proprietary studies were made to assess the impact of these changes to safety before the implementation of any reactor upgrades. Later, published results have demonstrated some of the points studied by IPEN, by other institutes, analyzing the influence of loss-of-flow and reactivity insertion accidents.[9] However, it was observed from subaquatic camera photographs the presence of oxidation on LFPs, as shown in Fig. 2. This was only present on specific LFPs of some SFA at its end of life, which was located in hot channels, after a long operation time at full power [5 MW(thermal)].

The study of corrosion of fuel plate aluminum clads[11–13] and minimization of oxide formation[14] is known under several scenarios, such as the pH influence[15,16] and its effects under heat transfer conditions for Al-6061 (Refs. 17, 18, and 19), which is the same alloy being used for more than 60 years in the IEA-R1 without major issues. The purpose of this work is not to discuss fuel chemistry or oxidation phenomena in Al-6061 alloys but rather to understand the fluid flow of the IEA-R1 research reactor core. Optimizing core flow dynamics can maximize heat removal in LFP, which is speculated can help reduce oxidation effects.

Figure 3 shows the dimensions of LFPs and SWCs in a cross-section view. The *xz*-plane opening region is responsible to cool LFP and visually has a larger pressure drop when compared to the α-region shown in Fig. 4. Additionally, it is important to note that the flow in the *yz*-direction is probably null since the assembly tolerance of the elements in the core suggests that this measure should be less than 1 mm. However, visual observations in the IEA-R1 core indicate that this dimension is heterogeneous. A considerable number of fuel elements physically touch

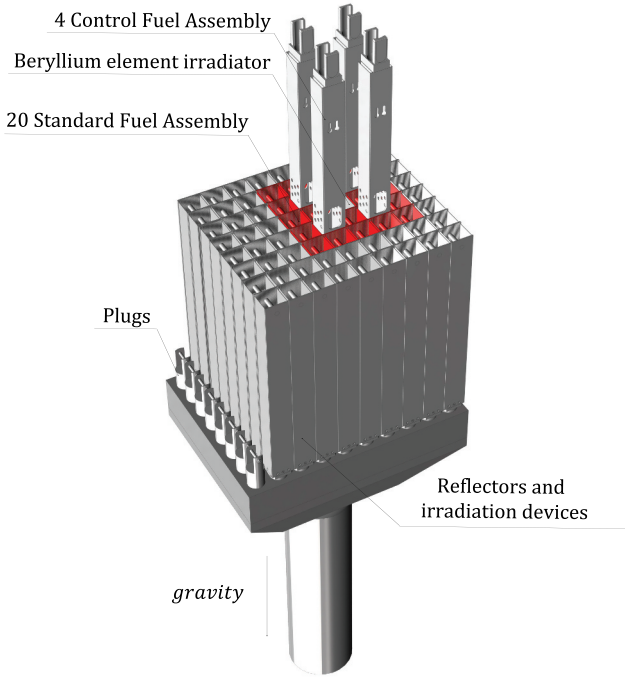

Fig. 1. Simplified three-dimensional model of the IEA-R1 reactor core.

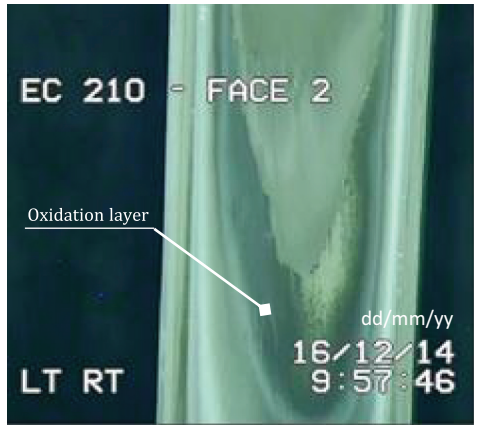

Fig. 2. Fuel assembly LFP photograph showing oxidation layer.[10]

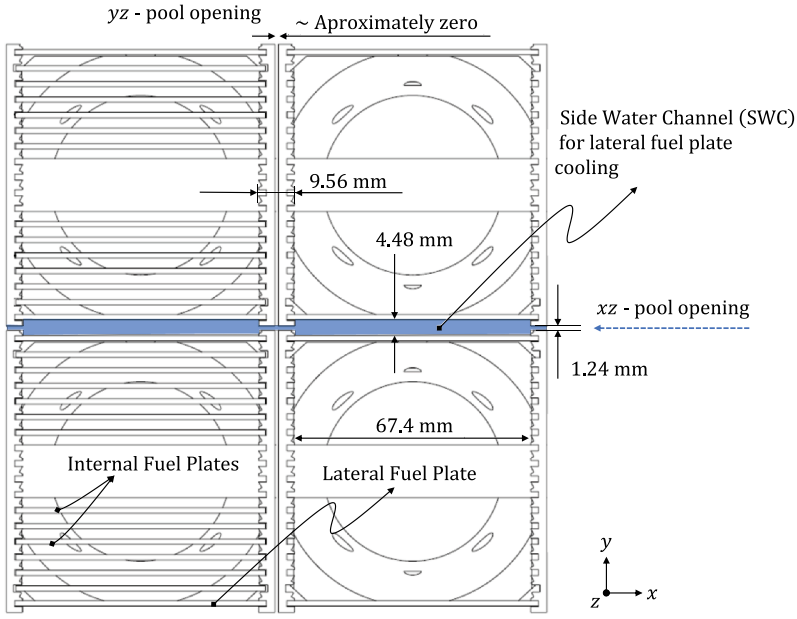

Fig. 3. Dimensions of the lateral channel.

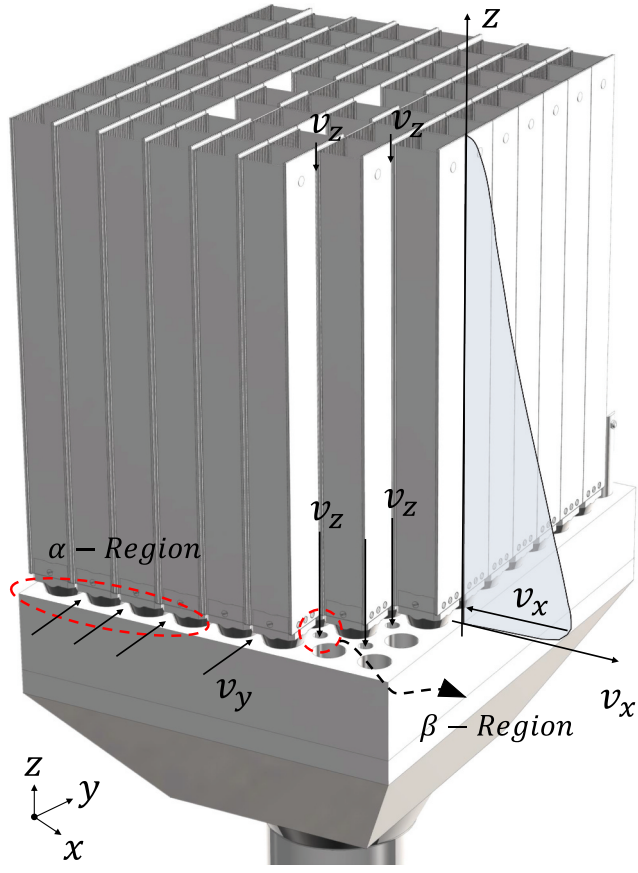

Fig. 4. Schematic velocity profile of SWC and core bypass regions.

each other, blocking the fluid flow in the *yz*-direction. Consequently, a larger fluid flow is expected to enter the α-region, which will be discharged among 56 orifices, highlighted as the β-Region in Fig. 4. This way, it is easier for coolant to enter the α-region rather than from SWCs (from both top v_z and sides v_x), which probably decreases LFP's cooling capacity. It is believed that this insufficient cooling in LFP can contribute to oxidation, as this effect was not observed in internal fuel plates for all other FAs.

Two studies were conducted to reduce oxide formation on LFPs as it was believed they were the only ones affected by high temperatures imposed by reactor power upgrade. The first was reducing the dispersion of nuclear fuel (U_3Si_2-Al) in LFPs by 50% (Ref. 20). Adjustments would be needed to achieve reactor criticality, and it was concluded that unfavorable effects would lead to this action. The second study focused on a geometrical modification of the core to improve cooling of LFPs by installing a channel box around the reactor core, limiting gaps and bypass fluid flow. The intent is to maximize mass flow to FAs instead of to unnecessary regions of the core. A channel box was first implemented for the German FRG-01 Reactor in 1999 (Ref. 21), shown in Fig. 5, which was designed for the purposes as described for the IEA-R1 reactor. However, because of the numerous instrumentation difficulties for measuring mass flow and fluid velocity in each FA, it was not possible to quantify the benefits of implementing such a device.[21]

To make progress in SFA's temperature recording during real operating conditions, the IPEN built an instrumented fuel assembly (IFA) in 2010, with 15 thermocouples.[22] The IFA led to the publication of an extensive experimental database[23] that allowed the validation and comparison of one-dimensional computer codes for the prediction of a slow loss-of-flow accident.[24] In the following year (2011), Umbehaun[25] with many other professionals at IPEN, designed and installed an Al-6061 channel box for the IEA-R1 similar to the German FRG-01 reactor.[21] Temperature recording results showed the direct influence of the channel box in IFA's fuel plate temperatures.[23] A temperature decrease between 7.7% to 27% was observed for many thermocouples.[23] However, as it was not possible to quantify the long-term influence of the channel box, it had a limited time operation, which did not allow observing the influence on oxide formation in LFP. In addition, it is not possible to record IFA-LFP's temperature as there are no thermocouples installed on LFPs due to the detachment possibility during movement of the IFA. In this way, a computational fluid dynamics (CFD) analysis may help to better understand the direct influence of the channel box in core flow dynamics and mass flow distribution.

Another important phenomenon related to the thermal-hydraulic safety criteria, which also justifies the performance of this study, is related to the mass flow distribution among all FAs. Because of the asymmetrical installation of FAs, one could expect a mass flow deviation among them, which could influence the temperature of individual FAs (Ref. 26). However, it is not known how significant this phenomenon can be. A numerical study quantifying mass flow distribution among FAs (Ref. 27) showed a deviation of 2% among FAs. However, other studies[28] showed that unequal distribution of mass flow is responsible for the corresponding unequal power distribution in the nuclear reactor.[29]

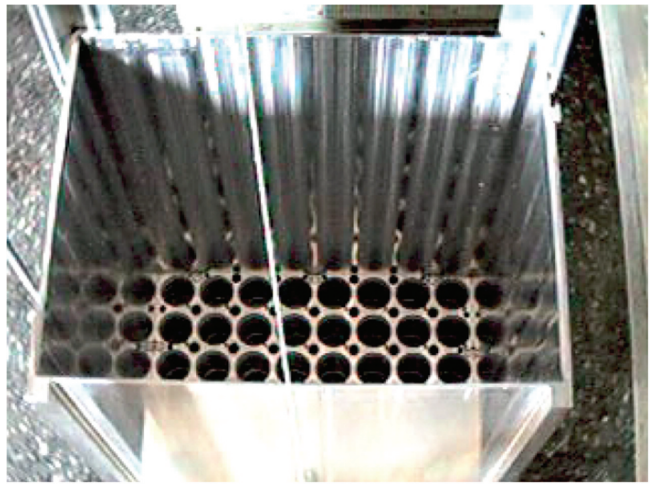

Fig. 5. German FRG-01 aluminum channel box.[21]

In addition, it is expected that SWCs have a complex three-dimensional behavior as they are open-to-pool in IEA-R1 and cannot be determined by a one-dimensional analysis without prior knowledge of the pressure loss behavior.

For these reasons, this paper describes the elaboration of a three-dimensional numerical analysis with the Ansys-CFX (Ref. 30) commercial software to study the flow characteristics and influence of the installation of a channel box surrounding the reactor core of IEA-R1. It will also be possible to understand the hydraulic advantages of using the channel box and compare the mass flow distributions for all SFAs. The proposed mathematical modeling includes a hybrid model in which the flow regions are fully discretized and other regions are replaced by one-dimensional modeling with an equivalent head loss coefficient, assuming a simplifying hypothesis of one-dimensional flow in these regions.

II. CFD ANALYSIS

This section will present all necessary assumptions made for the mathematical model of the IEA-R1 reactor core's simulation.

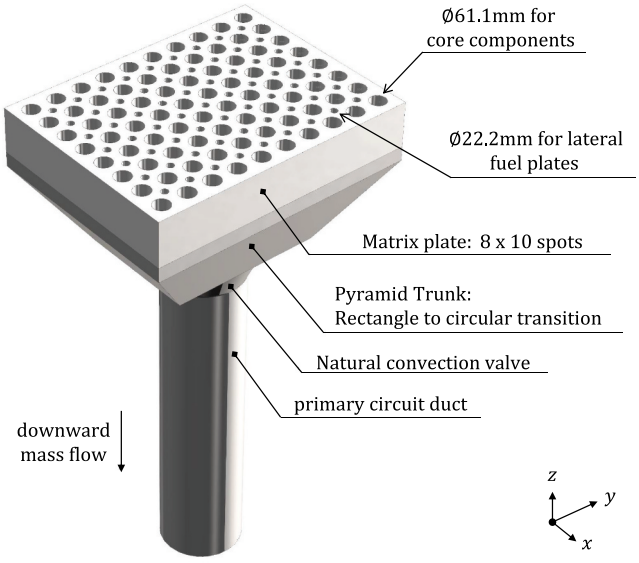

Fig. 6. Representation of the matrix plate and other components.

II.A. Boundary Conditions and Simplification Hypotheses

The IEA-R1 (Ref. 31) reactor core is mainly composed of 20 SFAs, 4 CFAs, one central beryllium irradiation device, reflector elements, irradiation elements for radioisotope production, temperature and pressure drop monitors, and other components. All these components are shown in a simplified way in Fig. 6. All the reactor core's elements are attached to a matrix plate, a rectangular metal device with 80 spots where all elements are attached and fixed. This matrix plate is directly attached to a pyramid trunk duct, a simple transformation of a rectangular cross section to a circular cross section, connecting to the primary circuit pump. This pyramid trunk is coupled with a natural convection valve (NCV), which is connected to the core by a pressure difference imposed by forced convection. This way, when the reactor is shut down, static pressure is null, and the NCV opens automatically, allowing stagnant water from the pool to enter the core to remove heat decay by natural convection.

All simplification hypotheses are presented as follows:

1. Since the whole reactor core is being analyzed, the discretization of internal regions of all SFAs and CFAs would require unnecessary computational expense as SFA's flow dynamics and validated head loss curve[7,32] are already known For this reason, SFAs and CFAs were replaced by a small portion of its outlet region (22.2-mm hole in Fig. 6) to an adaptive boundary condition, taking under consideration SFA and CFA hydraulic resistance using the Fig. 7 curve, also represented by Eq. (1):

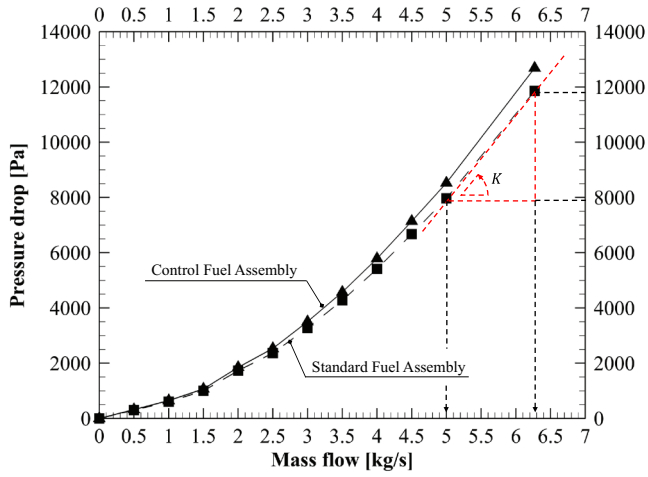

Fig. 7. Head loss of SFA (Ref. 7) and CFA.

$$K = \frac{2\Delta P \rho A_{nozzle}^2}{\dot{m}^2} \quad . \tag{1}$$

2. The same methodology of the SFA's study[7] was repeated for the CFA, and an average 7% higher head loss was adopted in this study (Fig. 7).

Therefore, all SFA and CFA head losses are considered in Ansys-CFX as a unidimensional pressure drop coefficient K, as a function of the pressure drop curve δp and mass flow rate $\dot{m}$, with a constant density ρ and outlet nozzle area of FAs, obtained from Fig. 6. In this way, we can include the hydraulic resistance curve of each SFA and CFA in the core model without the need for internal modeling of each FA. The only information required is the fluid density ρ (in kg/m^3) and a cross section A_{nozzle} (in m^2).

3. The other components of the reactor core that do not require cooling have been suppressed because they have no effect on hydrodynamics. These include irradiation elements, reflectors, neutron flux meters, pressure gauges, fission chambers, and other components.

4. The SWCs between the FAs (xz-plane) (Fig. 3) were not simplified; all different thickness levels and lengths were considered and discretized with the same validated patterns for head loss calculation as considered

in Scuro et al.[7] This means that cross flow between SWCs is taken under consideration.

5. The SWCs between the FAs (*yz*-plane in Fig. 3) were suppressed for two main reasons: (a) there is no significant flow in this region and (b) it is not directly responsible for cooling the fuel plates; i.e., the main flow occurs essentially in the *xz*-plane.

6. The region between the core components and the base of the matrix plate (see α-Region in Fig. 4) has minor simplifications, such as suppression of small wrinkles and regions where screw heads are located.

7. The NCV has been suppressed because it is relevant only after reactor shutdown. Therefore, since it is coupled when the reactor is operational, it has no influence on the fluid domain and flow dynamics.

8. The contact between the core components (FAs, control elements) with the matrix plate and other contacts is assumed to be perfect; i.e., leaks due to installation gaps are considered negligible.

9. The primary circuit pipe is just a 1-m simplified domain representation. Its function in this CFD model is only to impose the mass flow boundary condition of the primary pump.

10. The computational pool domain was not considered; this imposes that three-dimensional effects that occur at the entrance of the fuel elements or in the lateral channels are not captured. This simplification can influence the flow redistribution in the reactor core and increase the flow in the situation where the box is applied.

The computational domain is represented by a three-dimensional region through which fluid flows into the 64 SWCs, the opening region between the core elements and the matrix plate, and the pyramid stem with the primary channel section. For simplicity, the pyramid trunk and primary channel section are referred to as the coupling domain. The fluid is demineralized light water in the thermodynamic state of a subcooled liquid. The water inlet temperature is equal to the average operating temperature of the pool (32.7°C). The reactor core is located at a depth of about 6.89 m, the vertical distance from the surface of the pool to the top of the SWCs, resulting in an average hydrostatic pressure of 0.169 MPa. Water properties for the specified conditions were determined using the IAPWS-97 (Ref. 33). Figure 8 shows a representative schematic of some boundary conditions (the separation between the side channel domains, the opening to the pool, and the coupling domain).

In addition, some characteristics of the flow and boundary conditions are given as follows:

1. All surfaces in the computational domain are adiabatic and have no-slip wall conditions.

2. The average roughness of SWCs is 4 μm; other walls are 20 μm.

3. The primary suction flow is fixed at 211 kg/s.

4. The open pool regions have zero static pressure.

5. The free opening areas on the sides of the SWCs and the opening of the pool are considered as the wall for the box condition.

6. The pressure drop curves of the SFA and CFA were taken into the inlet area of each small representative extension of the outlet nozzle, i.e., the 50.8-mm cylinders, since the smaller ones of 22.2 mm represent the holes for cooling the SWCs.

7. The flow was considered isothermal.

III. MATHEMATICAL MODEL

The mathematical model considers single-phase light water flow in steady state. The hypotheses of (1) Newtonian fluid, (2) incompressible and isothermal flow, (3) validity of the Stokes' hypothesis,[34] and (4) negligible influence of viscous dissipation are assumed. Thus, the equations for conservation of mass and momentum are described by Eqs. (2) and (3), considering a Cartesian coordinate system x_i:

$$\frac{\delta U_i}{\delta x_i} = 0 \tag{2}$$

and

$$-\frac{1}{\rho}\frac{\partial p}{\partial x_i} + 2\frac{\partial}{\partial x_j}(\nu S_{ij}) = 0\,, \tag{3}$$

where

p = static pressure

ν = dynamic viscosity

U_i = velocity component in direction i

ρ = fluid density

S_{ij} = rate-of-strain tensor, represented by Eq. (4):

$$S_{ij} = \frac{1}{2}\left(\frac{\partial U_i}{\partial x_j} + \frac{\partial U_j}{\partial x_i}\right) . \quad (4)$$

In order to select a turbulence model suitable for the objectives of the work, it was necessary that the selected model not be prone to numerical instabilities since the geometry of the computational domain has several inlet regions with different dimensions and pressure drop coefficients. Another problem is the need for a high-quality near-wall discretization to correctly capture the boundary layer effects and subsequently determine the pressure drop in SWCs. For this reason, the two-equation $k-\omega$ model was used.[35] This model is based on the assumption that the time scale on which turbulent dissipation due to fluctuations occurs is proportional to the ratio between the turbulent dissipation rate and the turbulent kinetic energy $\omega \propto \frac{\epsilon}{k}$. This scale is called the rate of energy dissipation per unit volume and time ω.

The transport equations for the quantities k and ω are shown in Eqs. (5) and (6), respectively; the constants β', α'_1, β'_1, σ_k, and σ_{k_1} have values of 0.09, 5/9, 0.075, 2, and 2, respectively:

$$\rho\frac{\delta}{\delta x_i}(U_i k) = \frac{\delta}{\delta x_j}\left[\left(\mu + \frac{\mu_t}{\sigma_k}\right)\frac{\delta k}{\delta x_i}\right] + P_k - \beta'\rho k\omega \quad (5)$$

and

$$\rho\frac{\delta}{\delta x_i}(U_i \omega) = \frac{\delta}{\delta x_i}\left[\left(\mu + \frac{\mu_t}{\sigma_{\omega_1}}\right)\frac{\delta \omega}{\delta x_i}\right] + \frac{\omega}{k}\left[(\alpha'_1 P_k) - \beta'_1 \rho k\omega\right] . \quad (6)$$

The turbulent viscosity μ_t is obtained by Eq. (7), and P_k is the term of turbulence production due to viscous forces and is defined by Eq. (8):

$$\mu_t = \rho\frac{k}{\omega} \quad (7)$$

and

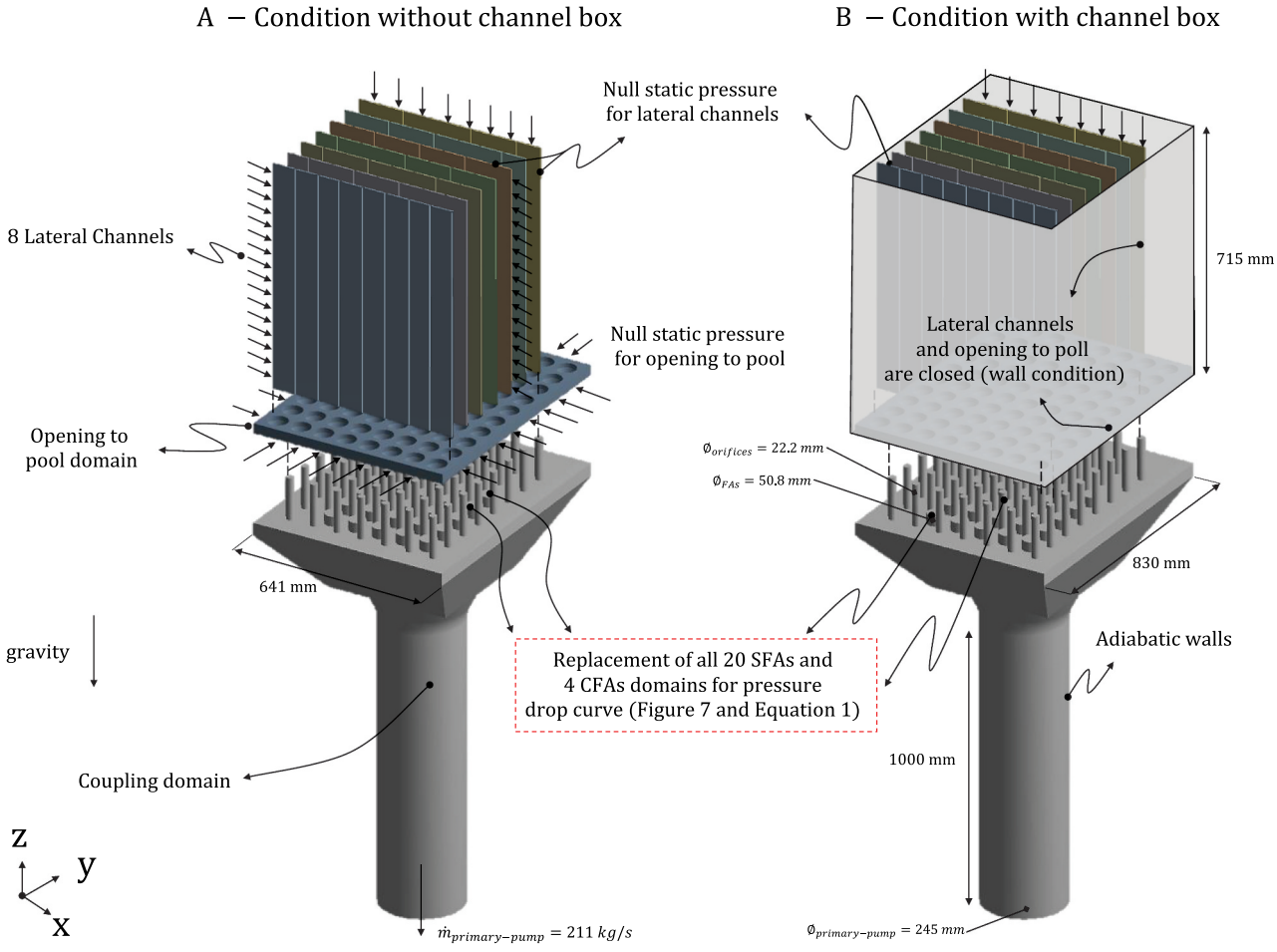

Fig. 8. Representation of simulated computational domains.

$$P_k = \mu_t \left(\frac{\delta U_i}{\delta x_j} + \frac{\delta U_j}{\delta x_i} \right) \frac{\delta U_i}{\delta x_j} \ . \quad (8)$$

The standard $k - \omega$ turbulence model was adopted since it provided a stable solution process for a computational domain that has several thin walls being connected to a bigger domain, which needed high discretization near the wall to correctly capture boundary layer effects. In addition, mesh parameters for SWCs were based on validated parameters for the presented FA's internal water channel mesh for pressure drop calculation.[7]

IV. DISCRETIZATION AND VERIFICATION

To correctly capture the fluid dynamics behavior, any discretization must be accompanied by a careful study of the mesh. In the analysis of the mesh density, a successive refinement was carried out, setting the same boundary conditions and applying the techniques proposed in the literature.[36,37] The computational domain has a relatively complex geometry and regions with very different dimensions. Some regions have relatively small dimensions compared to others. Therefore, the study of the grid was divided into several parts as shown in Fig. 9, where Region A is the SWC; Region B is the fluid domain open-to-pool; and Region C is the matrix plate, pyramid trunk, and primary circuit pipe fluid domain. This way, the analysis of the quantities chosen as monitoring parameters for successive refinement would not cause some regions to be obscured by others (this behavior could occur if a single mesh were used for the entire domain). In the study of each mesh in each region, the boundary conditions on some surfaces were chosen to simulate the coupling between regions. In this situation, the values of the quantities found in each simulation are parameters used to study the convergence of the mesh and should not be used to understand the real flow.

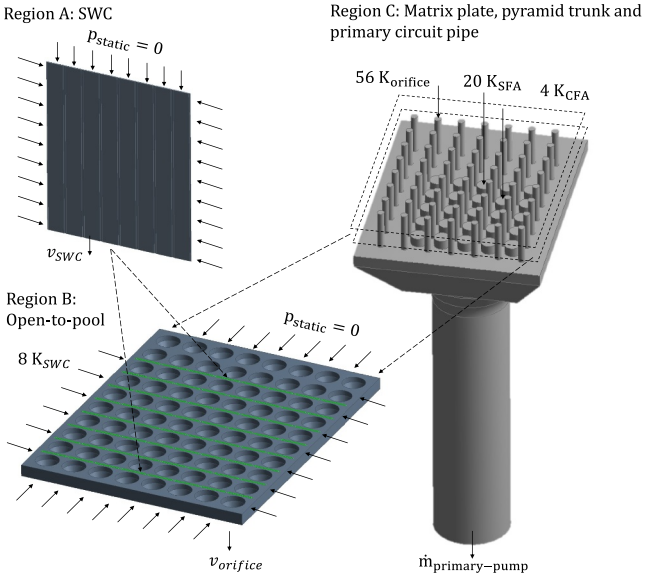

Fig. 9. Individual boundary conditions for domains to determine spatial discretization. Region A: SWC; Region B: region open to pool; and Region C: matrix plate, pyramic trunk, and primary circuit pipe.

A schematic representation of the boundary conditions used in this process can be seen in Fig. 9 in each of the computational domains. The numerical convergence process begins with the simulation of the SWC (Fig. 9, Region A), with opening conditions for the upper and side regions, followed by the specification of an average velocity in the lower region of the side channel v_{SWC}. Therefore, the ratio K between mass flow and pressure drop is calculated by Eq. (1), which provides an estimate of K_{SWC}. This dimensionless quantity is imposed on the contact regions between the SWCs and the opening domain for the pool (Fig. 9, Region B) to account for the pressure drop without requiring coupling. The inlet regions for the pool are considered with a static pressure of zero, and the flow is done by imposing an average velocity for each of the 56 orifices of the matrix plate $v_{orifices}$ in Fig. 9, Region C. Again, the constant K for the opening to the pool region is obtained, resulting in $K_{orifice}$. Finally, the dimensionless $K_{orifice}$, K_{SFA}, and K_{CFA} are applied to the respective regions for the coupled domain with a fixed flow rate of 211 kg/s for the primary channel.

Spatial discretization is defined when the deviations in the properties/quantities chosen for this purpose (mass flow and pressure drop) are less than 0.2% (value arbitrarily defined as a precision target) compared to the previous simulation. When this target is achieved, the discretization is considered independent of the results. This process was performed for each domain to ensure the lowest possible computational effort. SWCs have an exclusively hexahedral mesh that is not uniformly structured, allowing for a high number of near-wall elements necessary to adequately capture the boundary layer. The mesh parameters for this region can be found in Table I.

The same method used for SWCs was also applied in the region of the pool opening and in the coupling domain. However, because of the complexity of the geometry, a tetrahedral mesh with unstructured prismatic elements was used. The final parameters for these regions are listed in Table II.

To illustrate the monitoring process, to provide a numerical verification of the process, Fig. 10 shows the responses obtained for each domain and the analysis characteristics (mass flow for each domain and pressure drop for each

TABLE I

Spatial Discretization for the SWC

	$\delta_{thickness}$[a]	δ_{width}[b]	δ_{length}[c]	Number of Elements
Mesh N.1	8	8	36	26 625
Mesh N.2	11	11	51	70 000
Mesh N.3	15	15	71	201 250
Mesh N.4	21	21	101	526 250
Mesh N.5	30	30	142	1 475 000
Mesh N.6	42	42	200	4 064 000

[a]Number of divisions in each SWC thickness (4.48 mm).
[b]Number of divisions in each SWC width (67.40 mm).
[c]Number of divisions in each SWC length (725 mm).

TABLE II

Spatial Discretization for Coupling Domain and Opening to Pool

	Body Size (mm)	All Face Sizing (mm)	Thickness of Prismatic Layer (mm)	Number of Prismatic Layers	Number of Elements
Opening to pool	4	2	3	7	16 618 191
Coupling domain	15	3	4	7	8 132 500

domain). It is worth mentioning that the trend line between the points is only illustrative to check the influence of the discretization on the results.

The Grid Convergence Index (GCI) method[38] was calculated for each region adopting a proposed safety factor of 1.25. The maximum GCI obtained was 0.04%, which indicates a good mesh convergence.

The final mesh for all regions (A, B, and C) resulted in 36.58 millions of elements, 19.51 millions of nodes, for a total volume of $0.16 m^3$. Region A has an average element edge size varying from 15 to 0.5 mm, Region B has an average element edge size varying from 10 to 0.16 mm, and Region C has an average element edge size varying from 10 to 0.15 mm.

Figure 11 shows the entire domain in the section, with the first detail illustrating the connecting region between the three domains (side channel, opening to the pool, and coupled domain). The second detail illustrates the volumetric mesh of the side channel and the highest concentration of elements near the walls. Finally, the last detail illustrates the mesh aspect for the SFA and CFA regions (elements simulated as equivalent pressure drop). The mesh interfaces guarantee the conservation of the transported quantities (mass, momentum, or transport variables of the turbulence model).

The steady-state numerical analyses were calculated until the root-mean-square residuals for the mass and momentum conservation equations were less than 10^{-5}. Other parameters such as velocity and static pressure in several different spots were monitored to guarantee that the solution converged as expected. As an additional criterion, all high-resolution (second-order) discretization schemes for advection and turbulence were used. Double-precision variables were also imposed to reduce truncation errors.

V. RESULTS

The distribution of coolant flow in the reactor core is systematically changed with and without the channel box. To simplify the discussion, Fig. 12 shows a top view of the reactor core with the corresponding numbering of the flow regions. In Fig. 12, the SFAs are represented by gray circles from numbers 1 through 20, the CFAs are represented by circles from numbers 1 through 4, the internal SWCs are represented by small rectangular sections from numbers 1 through 64, and the side-channel suction holes are represented by small circles from numbers 1 through 56.

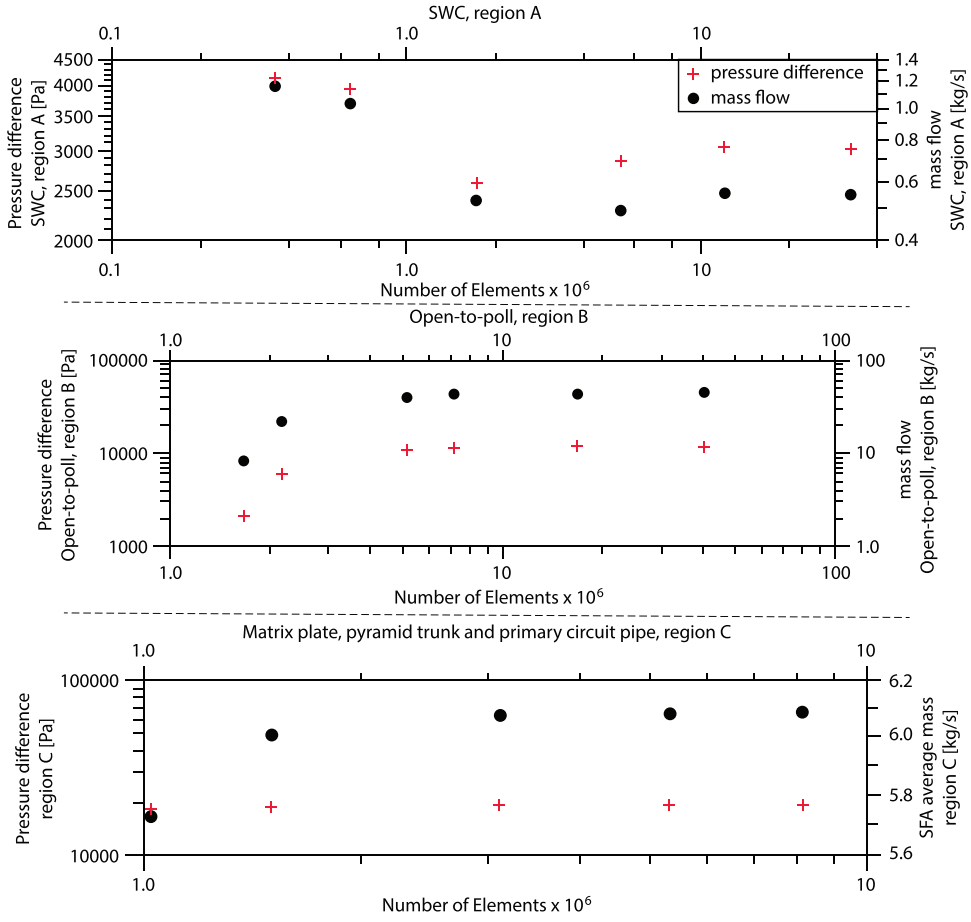

Fig. 10. Review of the spatial mesh: mass flow and pressure drop as a function of the number of elements (in millions) for the three regions studied.

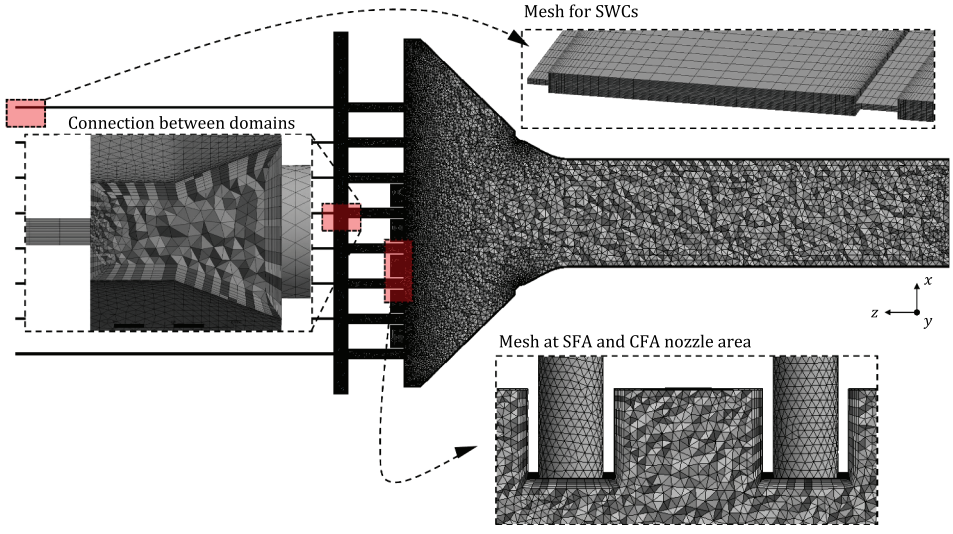

Fig. 11. Illustration of the final volumetric mesh of the computational domain.

V.A. Mass Flow Distribution in SFAs and CFAs

Figures 13 and 14 illustrate the distribution in both situations, without and with the channel box, with the respective standard deviations. It was not possible to observe a significant change in the spectrum of the flow distribution between the SFAs for both conditions, but there was a noticeable increase in the average flow, which

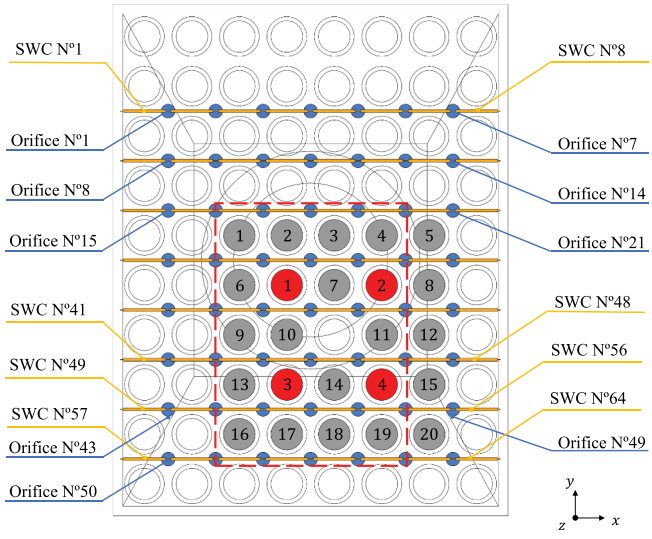

Fig. 12. Plan view of reactor core regions and spot numeration for SWC, orifices, SFAs, and CFAs.

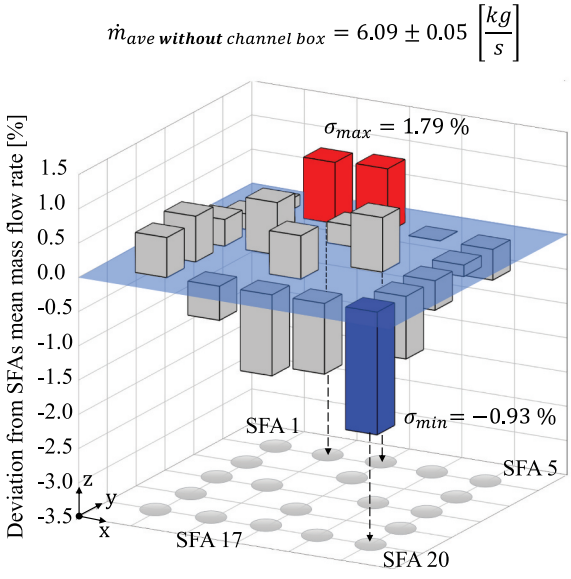

Fig. 13. Flow distribution between SFAs without channel box.

was increased by 12.64% (from 6.09 to 6.86 kg/s), with approximately the same deviation amplitude (± 0.05 kg/s). For the CFAs, the average mass flow rate in these assemblies increased from 5.90 (±0.02) kg/s to 6.63 (±0.01) kg/s, an increase of 12.37%, and negligible variations due to the small number of CFAs. This increase in the mass flow rate of the FAs due to the use of the box is promising because it is a clear indication that in this condition, if heat transfer does occur, the temperatures in the SFAs and CFAs are likely to be lower due to the 12.64% higher mass flow rates; however, this paper does

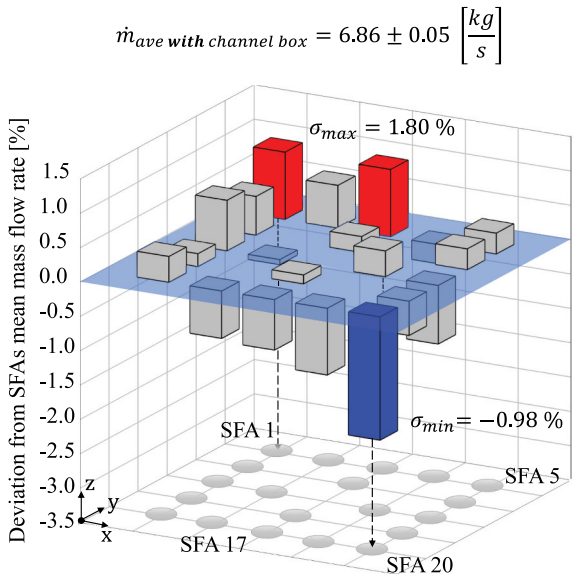

Fig. 14. Flow distribution between SFAs with channel box.

not consider heat transfer, and it is not possible to truly estimate its temperature decrease, but it is an expected behavior.

V.B. Velocity Distribution in SWCs

Since the main objective of this work is to investigate the effect of the installation of the channel box on the flow dynamics in the SWCs, a vector field was created for SWC numbers 49 through 56, for both situations, without the channel box (Fig. 15) and with the channel box (Fig. 16):

In the standard condition (Fig. 15), it was observed that the flow dynamics in these channels have a vector decomposition in two directions, v_x and v_z; i.e., the inner SWCs (SWC numbers 47 and 56) have a large influence of side flow v_x, but SWCs near the central part of the reactor core have predominantly a vector component oriented in the z-directionv_z. For the conditions shown in Fig. 15, the average velocity in the z-direction v_z is 0.78 m/s. Using the channel box (Fig. 16), there are virtually no velocity vectors in the x-direction v_x, and the average fluid velocity in the z-direction is 2.4 m/s. It was observed that the fluid dynamics is similar in all SWC numbers 47 through 56. And, this is an important point because the convective heat transfer between a surface and an adjacent fluid is directly proportional to the velocity field.

To illustrate the comparison of the velocity profiles in SWCs, the velocity profile v_z for the upper part of SWCs (numbers 47 through 56) was created to compare

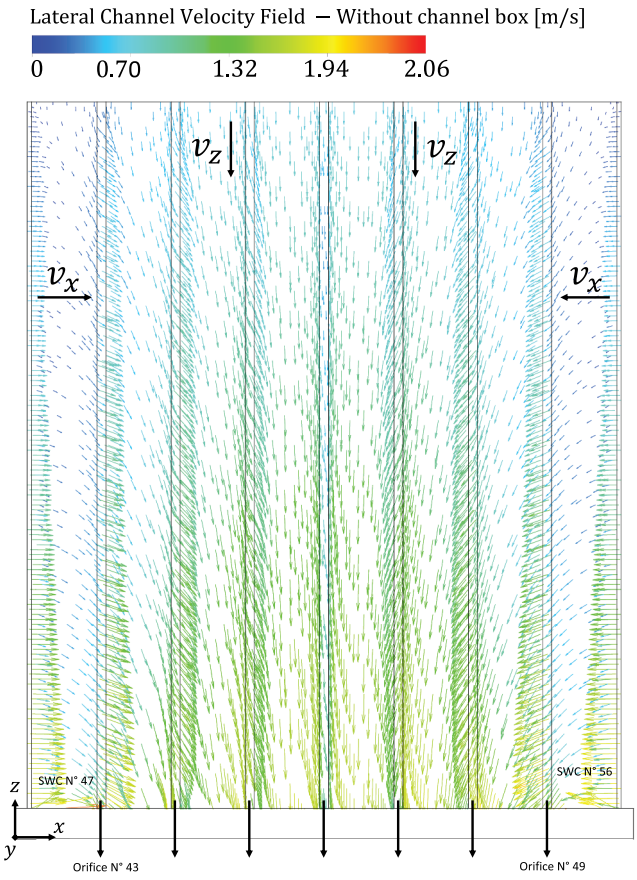

Fig. 15. Velocity vector field for SWC numbers 49 through 56 without channel box.

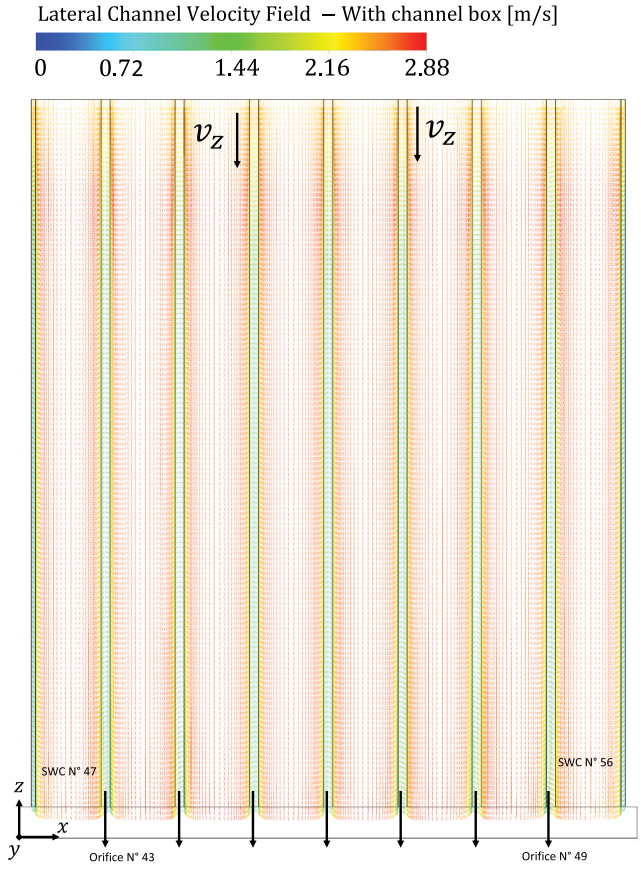

Fig. 16. Velocity vector field for SWC numbers 49 through 56 with channel box.

conditions without the channel box (Fig. 17) and with the channel box (Fig. 18).

It can be observed that in the condition without the channel box (Fig. 17), the downward velocity at the edge of the opening (near the pool) is practically zero. However, in the central part of the reactor core, the velocity v_z increases, which is quite similar to the velocity profiles in internal flows.

Such behavior was not observed with the channel box condition (Fig. 18) because all openings to the pool were closed. It is important to point out that there is a small connection between internal SWCs. Therefore, the velocity in the dashed lines in both situations in Figs. 17 and 18 is not zero (except in the contact of the fluid with the wall, i.e., contact with the channel box). Also, in this case a homogeneous, uniform, and similar behavior between the SWCs was observed. This indicates possible progress in the cooling of all SWCs. To illustrate the highly three-dimensional behavior of the velocity field for the condition without the channel box, a vector field was also created for the top and side openings of all SWCs, and it is shown in Fig. 19. It can be observed that the velocity vectors increase

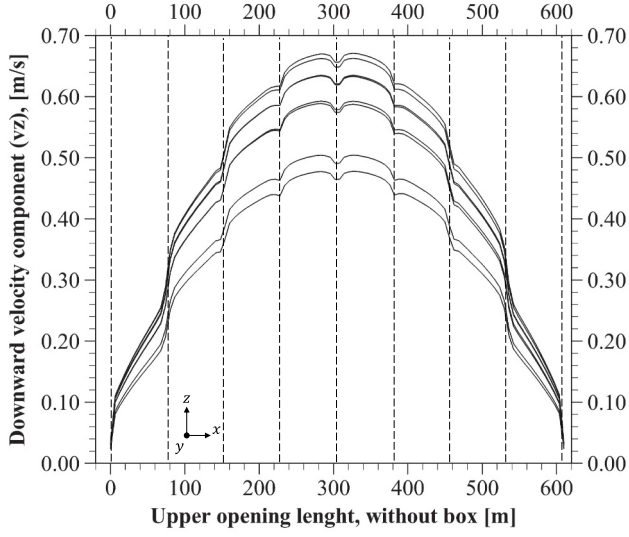

Fig. 17. Velocity profile in z-direction for condition without channel box for SWC numbers 49 through 56.

toward the central region of the core and are less intense in the peripheral regions, which drastically contributes to the heterogeneity of the cooling flow distribution in all SWCs.

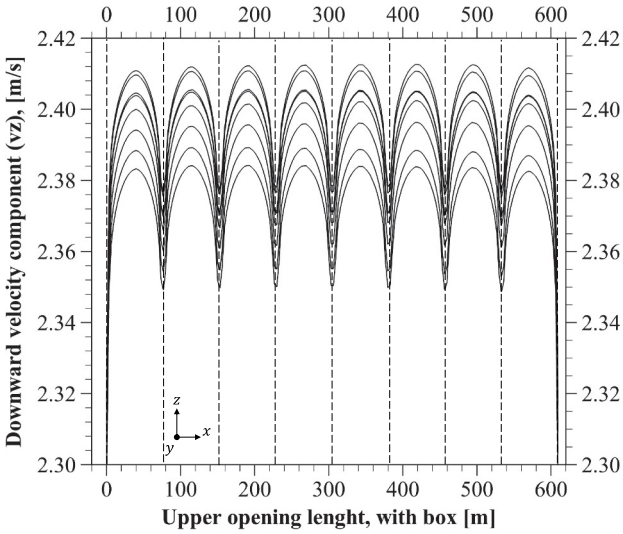

Fig. 18. Velocity profile in z-direction for condition with channel box for SWC numbers 49 through 56.

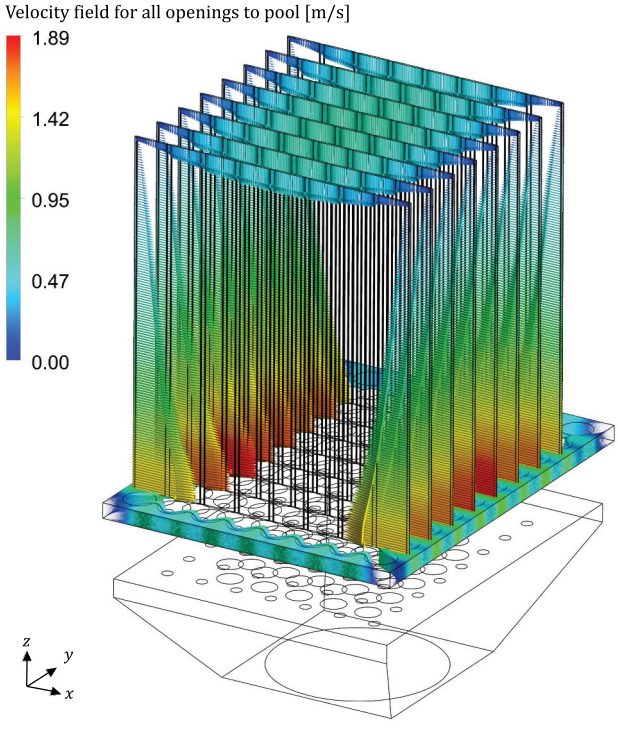

Fig. 19. Velocity vectors for the top and side openings.

V.C. Mass Flow Distribution in Orifices

The flow in SWCs and open-to-pool regions are due to the fluid entrancement exerted by the 56 holes of 22.2 mm of the matrix plate shown in Fig. 6 and indicated in Fig. 12. These orifices are responsible for the distribution of the flow in the SWCs. To illustrate the flow distribution between the orifices, the conditions with the channel box (Fig. 20) and without the channel box (Fig. 21) are presented.

Figures 20 and 21 show for both conditions the deviation from the orifice mean mass flow rate. For the condition without the channel box (Fig. 20), significant amplitude was identified (12.8% to −18.0%, totaling 30.8%) for an average mass flow rate of

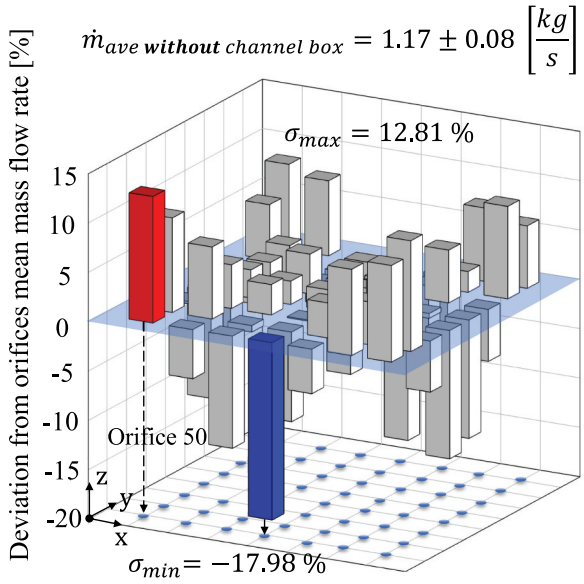

Fig. 20. Deviation from orifices mean mass flow rate without channel box.

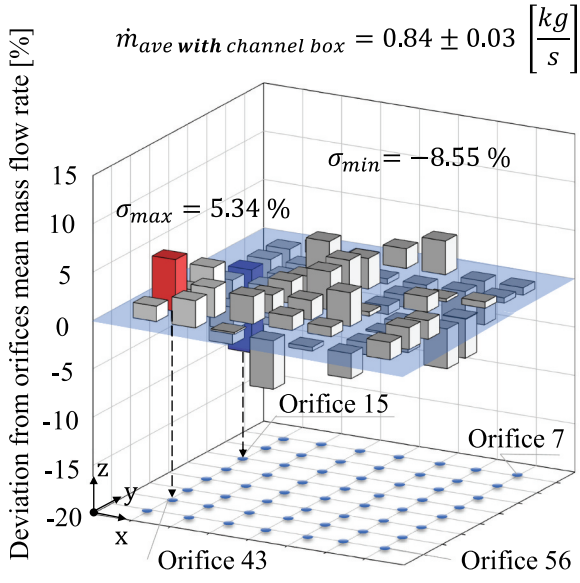

Fig. 21. Deviation from orifices mean mass flow rate with channel box.

1.17 kg/s. With the channel box (Fig. 21), the average mass flow rate decreased to 0.84 kg/s, and its deviation amplitude decreased to 5.3% to −8.6%, totaling 13.9%.

The decreased mass flow rate through the orifices was due to the increased hydraulic resistance imposed from the SWCs in comparison to the α-region (Fig. 4). However, the flow dynamics is different as shown from Figs. 15 and 16. The decreased deviation from the mean mass flow rate also resulted in a more homogeneous flow rate among all 56 orifices.

V.D. Summary of Channel Box Influence

The percentage of primary flow can be divided among the SFAs, CFAs, and SWCs, as shown schematically in Fig. 22 and presented with values in Table III. The pump mass flow was considered constant. The flow distribution can be idealized as a series of parallel channels such that an increase in the total pressure drop of a given group of elements directs the flow to regions of lower pressure drop. This behavior justifies the fact that the mass flow through the SFAs and CFAs increases when using the channel box.

The mass flow rates of the pump and orifices are determined by Eqs. (9) and (10), respectively:

$$\dot{m}_{orifices} = \dot{m}_{\mathrm{SWC}(top)} + \dot{m}_{\mathrm{SWC}(side)} + \dot{m}_{pool} \tag{9}$$

and

$$\dot{m}_{pump} = \dot{m}_{\mathrm{SFAs}} + \dot{m}_{\mathrm{CFAs}} + \dot{m}_{orifices}. \tag{10}$$

In a more detailed view in Fig. 12, it can be observed that only 30 of 64 SWCs (dashed square in Fig. 4) are responsible to remove heat from SFAs and CFAs. These specific 30 channels correspond to an average (determined by numerical simulations) of 9.49 kg/s of the total flow through the core of the nuclear reactor under standard conditions and not 30.75 kg/s, from the proportional 31.10% for 30 of 64 SWCs observed from Table III.

In summary, for these SWCs, the scenario with the channel box presented a total increase from 9.49 to 22.15 kg/s, with uniform flow dynamics (see Figs. 15 through 18). Therefore, even if the mass flow rate in the orifices was higher without a channel box (as discussed in Sec. V.C), this fluid would not be removing heat from LFPs. This is because the largest amount of fluid is taken up by the side of the pool $\dot{m}_{pool}$, which is admitted into the lower part of the reactor core, crosses the orifices, and is passed through the prism trunk without participating in the heat exchange for the FAs.

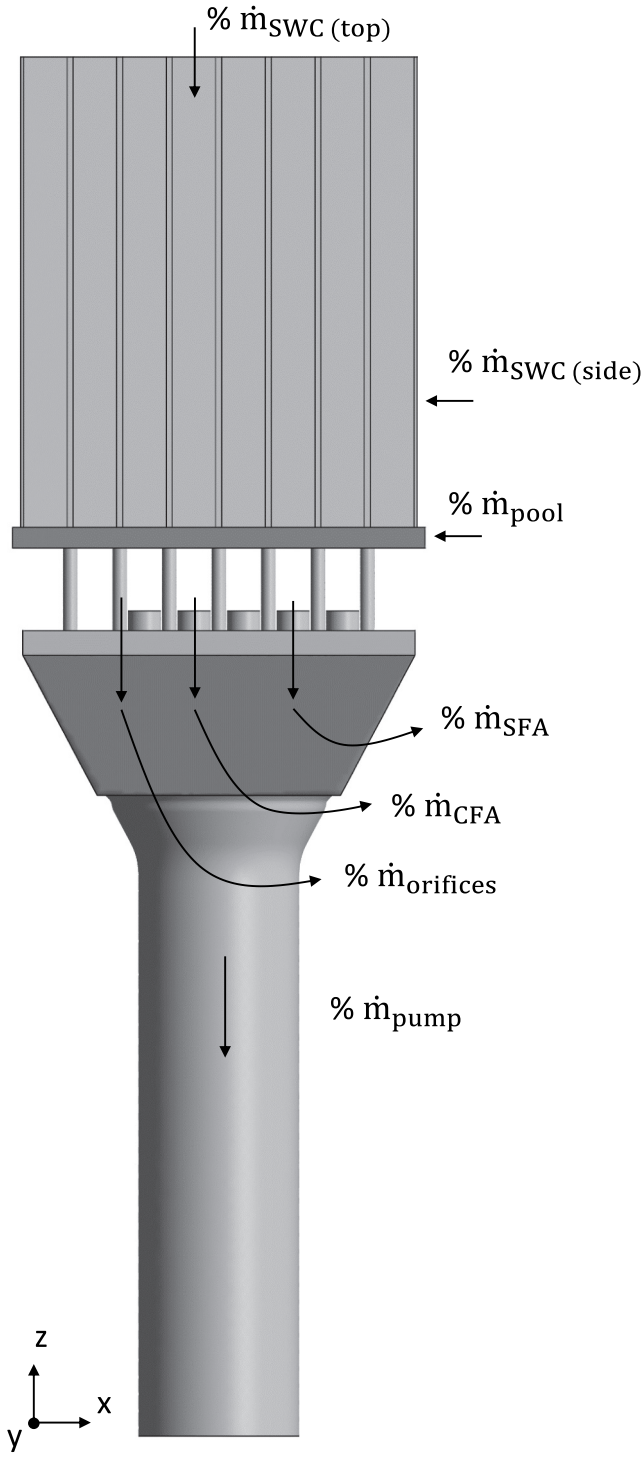

Fig. 22. Nomenclature and indication of the flow distribution in the nuclear reactor core.

TABLE III

Mass Flow Distribution with Channel Box Installation

Region	Without Channel Box	With Channel Box	Difference (kg/s)
$\dot{m}_{SWC(top)}$	3.90%	22.40%	39.0
$\dot{m}_{SWC(side)}$	5.80%	0.00%	−12.2
$\dot{m}_{pool}$	21.40%	0.00%	−45.2
$\dot{m}_{orifices}$	31.10%	22.40%	−18.4
$\dot{m}_{CFAs}$	11.20%	12.60%	3.0
$\dot{m}_{SFAs}$	57.70%	65.00%	15.4
$\dot{m}_{pump}$	100.00%	100.00%	0.0

VI. CONCLUSIONS

A numerical study was carried out on the implementation of a channel box in the core of a research nuclear reactor to reduce the flow deviations caused by the opening of the channels to the reactor pool and improving the flow available for cooling. The numerical results showed a significant change in the flow dynamics between the conditions with and without the channel box. The mathematical model for the turbulent incompressible flow used a hybrid numerical discretization for the analyzed regions. To simplify the reactor core model, the SFAs and CFAs were treated as elements with equivalent pressure drop without explicitly discretizing these regions. The results of the models indicate that the imposed geometric change provides advantages in cooling the FAs and the side fuel plates because of the greater mass flow available for cooling, which is a situation that must be taken into account when trying to lower the temperature of the side fuel plates and thus reduce the formation of oxides in the same plates. The presence of the channel box was responsible for directing the flow in the SWCs, which became almost vertical and descending. The presence of the channel box was also responsible for homogenization of the flow in all z-positions of the core.

The numerical results are consistent with the dynamics of parallel channels. Thus, increased pressure drop at a particular location directs mass flow to other regions. This behavior was observed in the comparison with and without the channel box. The effect contributes to the increase of the flux of SFAs and CFAs, and even with a lower mass flux in the orifices, the velocity field is on average oriented in a single direction (z-direction) and also has a higher modulus value. In conclusion, the use of a channel box to close the openings to the pool indicates a positive effect on the cooling of the core, which indicates that it can help to decrease the temperature at the LFPs and consequently decrease oxidation effects. For this reason, IPEN now has better arguments to design and implement a channel box in IEA-R1's reactor core.

Acknowledgments

The authors would like to thank both IPEN CNEN/SP and Ontario Tech University for the availability of the computer laboratory infrastructure and commercial software licenses. This study was funded by the IPEN CNEN/SP scholarship number 01341.000396/2018 and from the Canada Research Chairs program (950-231328) of the Natural Sciences and Engineering Research Council of Canada.

Disclosure Statement

The authors declare that they have no known competing financial interests or personal relationships that could have appeared to influence the work reported in this paper. The authors declare the following authorship contribution statement: Nikolas Lymberis Scuro: analysis, software, investigation, methodology, visualization, writing, review, and editing; Gabriel Angelo: methodology, analysis, conceptualization, writing, review, and editing; Edvaldo Angelo: analysis, conceptualization, writing, review, and editing; Markus Hans Alexander Piro: writing, review, editing, and resources; Walmir Maximo Torres: conceptualization and methodology; Pedro Ernesto Umbehaun: conceptualization, methodology, and supervision; Delvonei Alves de Andrade: conceptualization, supervision, and resources.

ORCID

N. L. Scuro http://orcid.org/0000-0002-4258-6607
G. Angelo http://orcid.org/0000-0002-1046-8657
E. Angelo http://orcid.org/0000-0001-7840-285X
M. H. A. Piro http://orcid.org/0000-0003-4721-3233
P. E. Umbehaun http://orcid.org/0000-0002-2887-0759
W. M. Torres http://orcid.org/0000-0002-7897-4783
D. A. Andrade http://orcid.org/0000-0002-6689-3011

References

1. Research Reactor Database (RRDB) website, International Atomic Energy Agency; https://nucleus.iaea.org/rrdb/#/home (accessed Jan. 22, 2022).
2. A. HAINOUN, N. GHAZI, and B. M. ABDUL-MOAIZ, "Safety Analysis of the IAEA Reference Research Reactor

During Loss of Flow Accident Using the Code MERSAT," *Nucl. Eng. Des.*, **240**, *5*, 1132 (2010); https://doi.org/10.1016/j.nucengdes.2010.01.001.

3. A. SALAMA, "CFD Investigation of Flow Inversion in Typical MTR Research Reactor Undergoing Thermal–Hydraulic Transients," *Ann. Nucl. Energy*, **38**, *7*, 1578 (2011); https://doi.org/10.1016/j.anucene.2011.03.005.
4. S. E.-D. EL-MORSHEDY, "Prediction, Analysis and Solution of Flow Inversion Phenomenon in a Typical MTR Reactor with Upward Core Cooling," *Kerntechnik*, **75**, *6*, 342 (2010); https://doi.org/10.3139/124.110110.
5. S. E.-D. EL-MORSHEDY, "Thermal-Hydraulic Modeling and Analysis of a Tank in Pool Reactor for Normal Operation and Loss of Flow Transient," *Prog. Nucl. Energy*, **61**, 78 (2012); https://doi.org/10.1016/j.pnucene.2012.07.005.
6. T. HAMIDOUCHE et al., "Dynamic Calculations of the IAEA Safety MTR Research Reactor Benchmark Problem Using RELAP5/3.2 Code," *Ann. Nucl. Energy*, **31**, *12*, 1385 (2004); https://doi.org/10.1016/j.anucene.2004.03.008.
7. N. L. SCURO et al., "RANS-Based CFD Calculation for Pressure Drop and Mass Flow Rate Distribution in an MTR Fuel Assembly," *Nucl. Sci. Eng.*, **195**, *4*, 349 (2021); https://doi.org/10.1080/00295639.2020.1825306.
8. "Research Reactor Modernization and Refurbishment," No. 1625 in TECDOC Series, International Atomic Energy Agency (2009).
9. A. HAINOUN, N. GHAZI, and F. ALHABIT, "Simulation of LOFA and RIA for the IEA-R1 Research Reactor Using the Code MERSAT," *Ann. Nucl. Energy*, **35**, *11*, 2093 (2008); https://doi.org/10.1016/j.anucene.2008.05.013.
10. J. SILVA et al., "Standard Fuel Assemblies and Control Bars Visual Inspection of the IEA-R1 Reactor Core," in Proprietary Technical Report (only in Portuguese): CEN-PSE-IEAR1-127-00 RELT-001-00, IPEN-CNEN-SP (2015).
11. "Corrosion of Research Reactor Aluminium Clad Spent Fuel in Water," No. 418 in TECDOC Series, International Atomic Energy Agency (2003).
12. E. SHABER and G. HOFMAN, "Corrosion Minimization for Research Reactor Fuel," INL/EXT-05-00256, Idaho National Laboratory (2005).
13. "Corrosion of Research Reactor Aluminium Clad Spent Fuel in Water," No. 1637 in TECDOC Series, International Atomic Energy Agency (2010).
14. D. V. TORDOYA, R. HADDAD, and R. AMORUSO, "Oxidation of Aluminum Plates MTR Fuel in Thermal Transfer Conditions," *Procedia Mater. Sci.*, **9**, 604 (2015); https://doi.org/10.1016/j.mspro.2015.05.036.
15. S. L'HARIDON-QUAIREAU et al., "Effects of Temperature and pH on Uniform and Pitting Corrosion of Aluminium Alloy 6061-T6 and Characterisation of the Hydroxide Layers," *J. Alloys Compd.*, **833**, 155146 (2020); https://doi.org/10.1016/j.jallcom.2020.155146.
16. S. PAWEL, D. FELDE, and R. PAWEL, "Influence of Coolant pH on Corrosion of 6061 Aluminum Under Reactor Heat Transfer Conditions," ORNL/TM–13083, Oak Ridge National Laboratory (1995).
17. R. PAWEL et al., "The Corrosion of 6061 Aluminum Under Heat Transfer Conditions in the ANS Corrosion Test Loop," *ASM Structural Materials Data Demonstration Project*, ASM (2013).
18. H.-S. SHIM et al., "Effect of Aluminum Oxide Coated on Fuel Cladding Surface on Crud Deposition in Simulated PWR Primary Water," *Ann. Nucl. Energy*, **121**, 607 (2018); https://doi.org/10.1016/j.anucene.2018.08.022.
19. Y. S. KIM et al., "Oxidation of Aluminum Alloy Cladding for Research and Test Reactor Fuel," *J. Nucl. Mater.*, **378**, *2*, 220 (2008); https://doi.org/10.1016/j.jnucmat.2008.06.032.
20. I. A. RIOS et al., "Uranium Density Reduction on Fuel Element Side Plates Assessment," *Proc. International Nuclear Atlantic Conf. (INAC)*, Belo Horizonte, Brazil, October, Vol. 1, p. 1 (2011).
21. P. SCHREINER and W. KRULL, "The New Compact Core Design of the FRG-1," *Proc. Int. Mtg. Reduced Enrichment for Research and Test Reactors (RERTR)*, Budapest, Hungary, October, INIS-XA-C-003, Vol. 1, p. 1, International Atomic Energy Agency (1999).
22. M. DURAZZO et al., "Procedures for Manufacturing an Instrumented Nuclear Fuel Element," *Prog. Nucl. Energy*, **113**, 166 (2019); https://doi.org/10.1016/j.pnucene.2019.01.021.
23. "Research Reactor Benchmarking Database: Facility Specification and Experimental Data," No. 480 in Technical Reports Series, International Atomic Energy Agency (2015).
24. A. HAINOUN et al., "International Benchmark Study of Advanced Thermal Hydraulic Safety Analysis Codes Against Measurements on IEA-R1 Research Reactor," *Nucl. Eng. Des.*, **280**, 233 (2014); https://doi.org/10.1016/j.nucengdes.2014.06.041.
25. P. E. UMBEHAUN, "Desenvolvimento de um elemento combustível instrumentado para o reator de pesquisa IEA-R1," PhD Thesis, Universidade de São Paulo, Instituto de Pesquisas Energétias e Nucleares (2016).
26. W. TIAN et al., "Development of a Thermal-Hydraulic Analysis Code for CARR," *Ann. Nucl. Energy*, **32**, *3*, 261 (2005); https://doi.org/10.1016/j.anucene.2004.09.003.
27. Y. BAE, Y. I. KIM, and C. T. PARK, "CFD Analysis of Flow Distribution at the Core Inlet of SMART," *Nucl. Eng. Des.*, **258**, 19 (2013); https://doi.org/10.1016/j.nucengdes.2013.02.003.

28. Z. CHEN et al., "Study of Core Flow Distribution for Small Modular Natural Circulation Lead or Lead-Alloy Cooled Fast Reactors," *Ann. Nucl. Energy*, **72**, 76 (2014); https://doi.org/10.1016/j.anucene.2014.04.032.

29. G. XIA, G. SU, and M. PENG, "Analysis of Flow Distribution in Plate-Type Core Affected by Uneven Inlet Temperature Distribution," *Ann. Nucl. Energy*, **92**, 333 (2016); https://doi.org/10.1016/j.anucene.2016.01.044.

30. "Ansys CFX-Pre-User's Guide," Vol. 13, ANSYS, Inc. (2013).

31. P. UMBEHAUN et al., "IEA-R1 Nuclear Reactor: Facility Specification and Experimental Results," International Atomic Energy Agency (2015).

32. T. HA and W. J. GARLAND, "Hydraulic Study of Turbulent Flow in MTR-Type Nuclear Fuel Assembly," *Nucl. Eng. Des.*, **236**, *9*, 975 (2006); https://doi.org/10.1016/j.nucengdes.2005.10.004.

33. W. WAGNER et al., "The IAPWS Industrial Formulation 1997 for the Thermodynamic Properties of Water and Steam," *J. Eng. Gas Turbines Power*, **122**, *1*, 150 (Jan. 2000); https://doi.org/10.1115/1.483186.

34. F. M. WHITE, *Viscous Fluid Flow*, McGraw Hill (1991).

35. D. C. WILCOX et al., *Turbulence Modeling for CFD*, Vol. 2, DCW Industries, La Canada, California (1998).

36. F. STERN et al., "Comprehensive Approach to Verification and Validation of CFD Simulations—Part 1: Methodology and Procedures," *J. Fluids Eng.*, **123**, *4*, 793 (July 2001); https://doi.org/10.1115/1.1412235.

37. R. V. WILSON et al., "Comprehensive Approach to Verification and Validation of CFD Simulations—Part 2: Application for Rans Simulation of a Cargo/Container Ship," *J. Fluids Eng.*, **123**, *4*, 803 (July 2001); https://doi.org/10.1115/1.1412236.

38. P. J. ROACHE, *Verification and Validation in Computational Science and Engineering*, Vol. 895, Hermosa, Albuquerque, New Mexico (1998).